Journal of Nuclear Materials 448 (2014) 33–42

Contents lists available at ScienceDirect

Journal of Nuclear Materials

journal homepage: www.elsevier.com/locate/jnucmat

Long-term microstructural stability of oxide-dispersion strengthened Eurofer steel annealed at 800 °C

K.D. Zilnyk [a], H.R.Z. Sandim [a,*], R.E. Bolmaro [b], R. Lindau [c], A. Möslang [c], A. Kostka [d], D. Raabe [d]

[a] Escola de Engenharia de Lorena – USP, 12600-970 Lorena, SP, Brazil
[b] Instituto de Física Rosario, CONICET-UNR, 2000 Rosario, Argentina
[c] Karlsruher Institut für Technologie, KIT, IAM-AWP, D-72061 Karlsruhe, Germany
[d] Max-Planck Institut für Eisenforschung, MPI-E, D-40237 Düsseldorf, Germany

GRAPHICAL ABSTRACT

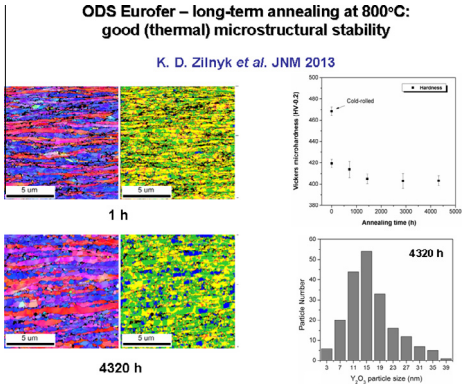

ARTICLE INFO

Article history:
Received 26 August 2013
Accepted 20 January 2014
Available online 27 January 2014

ABSTRACT

Oxide-dispersion strengthened ferritic martensitic steels such as ODS-Eurofer grade are good candidates for structural applications in future fusion power reactors. Long-term annealing treatments in vacuum were carried out in cold-rolled samples (80% reduction in thickness) from 1 h up to 4320 h (6 months) at 800 °C, i.e. the maximum temperature in the ferritic phase field, to follow its softening behavior. The microstructural stability of this steel was mapped using several characterization techniques including scanning electron microscopy, transmission electron microscopy, electron backscatter diffraction, Vickers microhardness testing, X-ray diffraction texture measurements, low-temperature electrical resistivity, and magnetic coercive field measurements. ODS-Eurofer steel displays good microstructural stability. Discontinuous recrystallization occurs at the early stages of annealing resulting in a low volume fraction of recrystallized grains. Extended recovery is the predominant softening mechanism at this temperature for longer times.

1. Introduction

Reduced-activation ferritic–martensitic (RAFM) steels have a large number of interesting properties for applications in the first wall of future nuclear fusion reactors as well as in Generation IV fission reactors. Some of these properties include reduced void swelling, high resistance to nuclear transmutation, high mechanical strength even at high temperatures, and reasonable ductility when compared to the austenitic steels currently used in fission reactors such as 316-LN stainless steel [1–5]. One limitation for the application of RAFM steels is the poor creep resistance above 550 °C, but

* Corresponding author. Tel.: +55 12 3159 9916; fax: +55 12 3153 3006.
E-mail addresses: hsandim@demar.eel.usp.br, hsandim@uol.com.br (H.R.Z. Sandim).

http://dx.doi.org/10.1016/j.jnucmat.2014.01.032
0022-3115/

this drawback can be surpassed by employing oxide dispersion strengthened (ODS) RAFM steels [5]. It is well known that a homogeneous dispersion of fine and stable particles is very effective to reduce both the dislocation mobility and the grain boundary velocity, critical parameters for creep strength, increasing the operating temperature of ODS-Eurofer steel up to, at least, 650 °C [5–7].

Microstructural stability of this class of steels is a prerequisite to avoid the deterioration of their mechanical properties in structural components exposed for long times to a very hostile environment, which includes high neutron fluxes at high temperatures, as the one expected during operation of future fusion reactors. In particular, the yet-unknown long-term softening behavior of this steel in the cold-rolled condition is addressed in this investigation. It is worth mentioning that these conditions are far from those where neutron irradiation is present but the results are useful to understand the microstructural changes that take place at temperatures much above than the expected for normal operation, i.e. below 650 °C [5]. Furthermore, there are no irradiation facilities yet able to reproduce the expected severe conditions during operation of either ITER or DEMO reactors [8].

A key factor in the microstructure of this class of steel is the presence of a dispersion of Y_2O_3-based particles with sizes in the nm-range that are incorporated to the matrix during suitable powder metallurgy processing [9,10]. The oxide nanoparticles exert important Zener-type pinning effects on subgrain boundaries, preventing subgrain coarsening and, thus, the increase in subgrain boundary misorientation that would generate potential nuclei for primary (discontinuous) recrystallization. In some situations, it may suppress discontinuous recrystallization at homologous temperatures up to $0.9T_m$, where T_m is the melting point or *liquidus* temperature [11,12], and static recovery is responsible for most of the softening reported for this steel. If the pinning force [13,14] acting on the subgrain boundaries decreases, either due to particle coarsening (Ostwald ripening) or chemical modifications of the matrix (less solute drag), subgrain growth may occur, leading to a microstructure softened by *"extended recovery"* and, in some situations, by "*continuous recrystallization*". In the latter case, the resulting microstructure consists of equiaxed grains containing only small fractions of low angle boundaries (LABs) without the occurrence of nucleation and coarsening of recrystallization nuclei [15,16].

In previous works [17,18], the influence of the annealing temperature on the microstructure of annealed samples of both cold-rolled ODS-Eurofer and conventional (non-ODS) Eurofer-97 steels was reported. While cold-rolled samples of Eurofer-97 deformed to large strains underwent discontinuous recrystallization at temperatures of about 500 °C, recrystallization in a large extent was not observed in the ferritic field for similar cold-rolled samples of ODS-Eurofer [17,18] This result suggests strong pinning effects caused by oxide nanoparticles on dislocations and grain boundaries (either high and low angle characters). On the other hand, recent studies performed by Raman and Schäublin in ODS steels have shown significant softening even after annealing for 1 h [19]. It is worth mentioning that particle dissolution was observed in Ti-containing ODS steels even at moderate temperatures (600 °C). Contrastingly, the same authors have reported a much higher stability of Y_2O_3 particles in ODS steels annealed at temperatures up to 1000 °C [19].

Some papers on the influence of long-term exposures to high temperatures on the mechanical behavior of Eurofer-97 are found in the literature [5,20–24]. According to Fernandez [21,22] exposures up to 10,000 h close to the operational temperature (500–600 °C) did not result in significant degradation of tension and impact properties of Eurofer-97. The author also observed the coarsening of carbides. Creep experiments were conducted in similar temperatures up to 30,000 h and the results revealed a high level of stability and predictability [5,20,23,24]. Long exposures at higher temperatures (>700 °C) were found to increase the ductile-to-brittle transition temperature (DBTT) [20]. However, studies reporting the effects of long time thermal exposures on ODS-Eurofer are scarce in the literature. Lindau et al. [5] reported that creep tests were performed on such a material at temperatures between 600 and 700 °C up to rupture times of 10,000 h. The creep strength of ODS-Eurofer was found to be similar to those presented by Eurofer-97 at temperatures about 100 °C below.

In this study, we report and discuss the main results obtained on samples of ODS-Eurofer steel annealed at high temperatures in the ferritic field (800 °C) for very long times, with times ranging from 1 up to 4320 h (6 months) to evaluate its thermal (microstructural) stability, with emphasis on its recrystallization behavior. Although this temperature is higher than the one expected during service life, it is sufficiently high to promote accelerated annealing tests, helping to understand the softening behavior in this material. The microstructural evolution was investigated by means of electron backscatter diffraction (EBSD), X-ray diffraction (XRD) texture measurements, Vickers microhardness testing, coercive field, electrical resistivity, and transmission electron microscopy (TEM).

2. Experimental

2.1. Material

The ODS-RAFM steel investigated in this study, namely ODS-Eurofer, was developed and processed by former *Forschungszentrum Karlsruhe* (FZK), now termed *Karlsruher Institut für Technologie* (KIT) in cooperation with Plansee AG [5]. The processing route to obtain this material includes suitable powder metallurgy techniques followed by hot-isostatic pressing (HIP) and further hot rolling (finishing temperature of about 980 °C) to consolidate the material and is similar to that used in others oxide-dispersion strengthened materials like Ni- and Fe-based ODS superalloys like PM-1000 and PM-2000 grades [12,25]. More details are given elsewhere [5,26–28]. The chemical composition of the ODS-Eurofer steel is given in Table 1. The material was supplied in sheets with thickness of 6 mm in the tempered condition; i.e. a fully ferritic microstructure (720 °C for 2 h followed by air cooling). The sheets were cold-rolled to 80% thickness reduction in multiple passes. Samples were annealed in vacuum at 800 °C for times ranging from 1 h up to 4320 h (6 months), followed by air cooling. After mechanical polishing of the longitudinal section of samples, Vickers microhardness testing was performed using a load of 200 g for 30 s parallel to the rolling direction (ASTM E384–11e1). Ten measurements were performed in each sample.

Table 1
Chemical composition of ODS-Eurofer steel.

	Cr	W	Mn	V	Ta	Si	C	Y_2O_3
%- mass	8.92	1.11	0.408	0.193	0.081	0.111	0.071	0.3
	S	P	Nb	Mo	Al	Ti	N	Fe
ppm	31	105	2	37	36	7	278	Bal.

2.2. Microstructural characterization

EBSD measurements were performed in a JEOL-6500F field emission gun scanning electron microscope (FEG-SEM) by means of automated acquisition and indexing of Kikuchi patterns in a TSL system over areas of about $40 \times 60\ \mu m^2$ area using a step size of 40 nm [29,30]. Samples were mechanically ground to the middle layer in thickness and electrochemically polished for texture measurements. Texture measurements were performed in a MPD Philips diffractometer using Cu-Ka radiation, accelerating voltage of 40 kV and current of 30 mA. Orientation distribution functions (ODFs) were calculated from {1 1 0}, {2 0 0} and {2 1 1} pole figures using the WXpopLA software package (current Windows XP implementation by Bolmaro and co-workers) [31]. After mechanical grinding and double ion polishing on samples, transmission electron microscopy (TEM) images were collected using JEOL JEM-2200SS (MPIE) and Philips CM-30 (KIT) microscopes both operated at 200 kV. The size distribution of Y_2O_3 particles was evaluated by using image analysis software.

Electric and magnetic measurements were made at low temperature (4 K) using a Quantum Design EverCool II Physical Properties Measurement System (PPMS). Electrical resistivity was measured in samples parallel to the rolling direction, using the four-probe method with an applied voltage of 500 mV. The values of the magnetic coercive field were obtained from the hysteresis loops and they were calculated as the average magnetic field modulus required to reduce the material magnetization to zero after complete magnetic saturation [17,18]. The hysteresis loops were collected with magnetic fields up to 15 kOe, applied parallel to the rolling direction, using the following sweep rates, in order to optimize both the experimental time-length and the amount of collected data: 0.4 kOe/min for $|H| < 0.5$ kOe, 1.8 kOe/min for $0.5 < |H| < 5$ kOe and 10 kOe/min for $6 < |H| < 15$ kOe.

3. Results and discussion

3.1. Microstructure

The microstructure of ODS-Eurofer steel in the as-received (tempered) condition was reported in detail elsewhere [32–35]. It consists of a ferritic matrix with mean grain size of about 3 μm containing Cr-rich coarse $M_{23}C_6$-type particles with sizes above 100 nm and fine Y_2O_3 nanoparticles (<40 nm).

Phase stability of ODS-Eurofer after 6-months exposure at 800 °C was investigated and reported elsewhere [36]. Only coarse $M_{23}C_6$ with sizes in the range 100–600 nm and Y-based nanoparticles could be found using transmission electron microscopy. Besides carbon, iron, chromium, and tungsten were the major elements found in $M_{23}C_6$-type carbide particles in TEM [36]. Tungsten replaces some of the Cr atoms in the carbide structure. Neither Z- nor Laves phases were observed in the microstructure, with good agreement with the thermodynamic calculations (Thermo-Calc software coupled with TCFE 7 database [36]) for the annealing temperature used in this work.

The microstructure of ODS-Eurofer steel was imaged in detail using transmission electron microscopy. Fig. 1 shows its microstructure after annealing at 800 °C for 1 h. It is rather inhomogeneous since recovered and recrystallized areas are found in close vicinity (Fig. 1a). This feature has to do with the inhomogeneous distribution of stored energy from cold rolling (texture effects). Subgrains can also be noticed in Fig 1b. It shows the progress of recovery in this material. Dislocation boundaries are not perfect (not only geometrically necessary dislocations are present in the planar boundaries) and a high density of free dislocations can be noticed.

These features did not change significantly after 4320 h. The microstructure is inhomogeneous and it consists of recovered and recrystallized areas. The most important change is the degree of recovery observed in some regions in the microstructure. Fig. 2a shows elongated lamellar boundaries inherited from the deformation structure lying nearly parallel to the rolling direction (marked by the arrow). Y_2O_3 nanoparticles can also be noticed dispersed in the matrix. In other areas, subgrains and fine equiaxed grains are noticeable (Fig. 2b). Planar boundaries now are much more perfect displaying a much lower density of free dislocations within subgrains. These features can be noticed in detail in Fig. 2c where low angle and high angle boundaries (HAB) are shown. Contrastingly, in other areas the degree of recovery is incomplete when compared to the feature shown in Fig. 2b and areas with high dislocation density can still be found (Fig. 2d). A general view of the microstructure is displayed in Fig. 3a. This montage made with consecutive micrographs show a banded structure where recovered and recrystallized areas are present. Orientation effects are evident since recrystallization takes place preferentially within a given band where the stored energy was higher. A closer inspection shows coarse $M_{23}C_6$ (darker contrast) and Y_2O_3 nanoparticles (marked by arrows) in close vicinity (Fig. 3b).

The stability of oxide particles in ODS materials seems to be strongly dependent on their chemical composition [37]. The literature reports the stability of Y_2O_3 nanoparticles even at temperatures as high as 1300 °C [19,38]. ODS-Eurofer steel has a chemical composition similar to those where particle stability is reported. Previous works [34,39] show that the oxide particles in the ODS-Eurofer are typically Y_2O_3 due to its very low Ti content. Ramar and Schäublin reported a quite different behavior in a Ti-bearing ODS-steel [19], Complex Y-based Ti-containing oxide nanoparticles (e.g. $YTiO_5$ and $Y_2Ti_2O_7$) undergo dissolution even at fairly low temperatures such as 600 °C. On the other hand, other authors [10,40,41] reported a great stability of Y–Ti–O in temperatures up to 1100–1300 °C. Williams et al. reported that both Ti-bearing and Ti-free Y_2O_3 particles displayed similar coarsening rates at 1200 °C [42]. This issue is still unclear and a systematic and comprehensive study varying the composition of the oxide particles in ODS steels is not yet available in the literature.

Despite of the small number of particles counted in TEM micrographs (200 particles) in the present investigation, the particle size distribution of ODS-Eurofer steel annealed at 800 °C for 4320 h was evaluated (Fig. 3c). The mean Y_2O_3 particle size found in our investigation is 16.4 ± 7.3 nm, very close to the values reported by Eiselt et al. and Klimiankou et al. (about 12 nm) based on a much larger number of particles counted in TEM for the same steel in the tempered condition [39,43]. Therefore, based on these experimental results, significant dissolution or coarsening of the particles was not observed in ODS-Eurofer steel annealed at 800 °C.

EBSD maps corroborate the results found in TEM in a qualitative manner. Inverse pole figure (IPF) and Kernel average misorientation (KAM) maps are shown in Fig. 4. While IPF maps show the orientation of individual grains, KAM maps show the average misorientation angle between each pixel and its ten closest neighboring pixels. It is a useful technique employed to detect local orientation gradients caused by inhomogeneously stored energy in the deformed matrix [44]. The total and partition fractions for KAM (Fig 4) are given relative to the full 40×60 μm maps, but only cropped 12×12 μm IPF and KAM maps are presented for more transparent visualization. For longer annealing times, there is a noticeable decrease in the partitional fraction (which does not consider non-indexed areas such as carbides and grain boundaries) of misorientation angles above 2°, indicating that recovery processes are effective in the material [45].

The cold-rolled microstructure is shown in the IPF map in Fig 4(a). The deformed grains have elongated shape parallel to the roll-

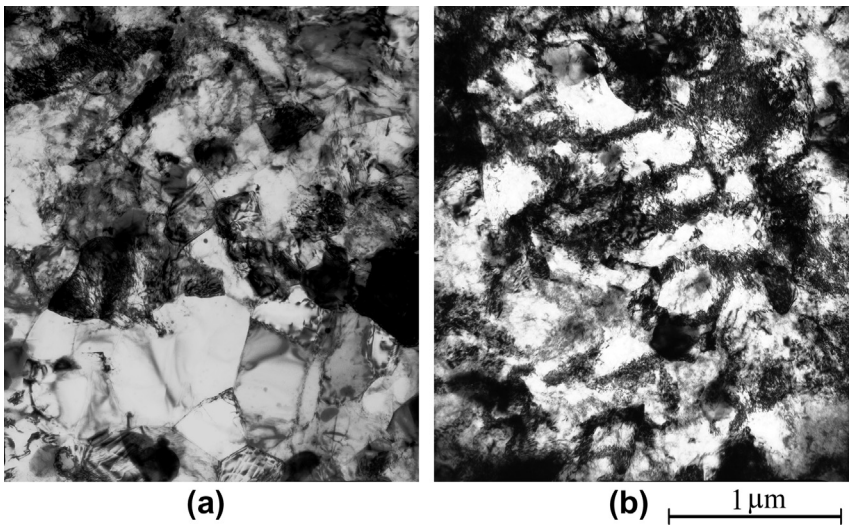

Fig. 1. TEM bright field images of ODS-Eurofer steel annealed at 800 °C for 1 h. The scale bar is the same for both micrographs. The rolling direction is parallel to the scale bar.

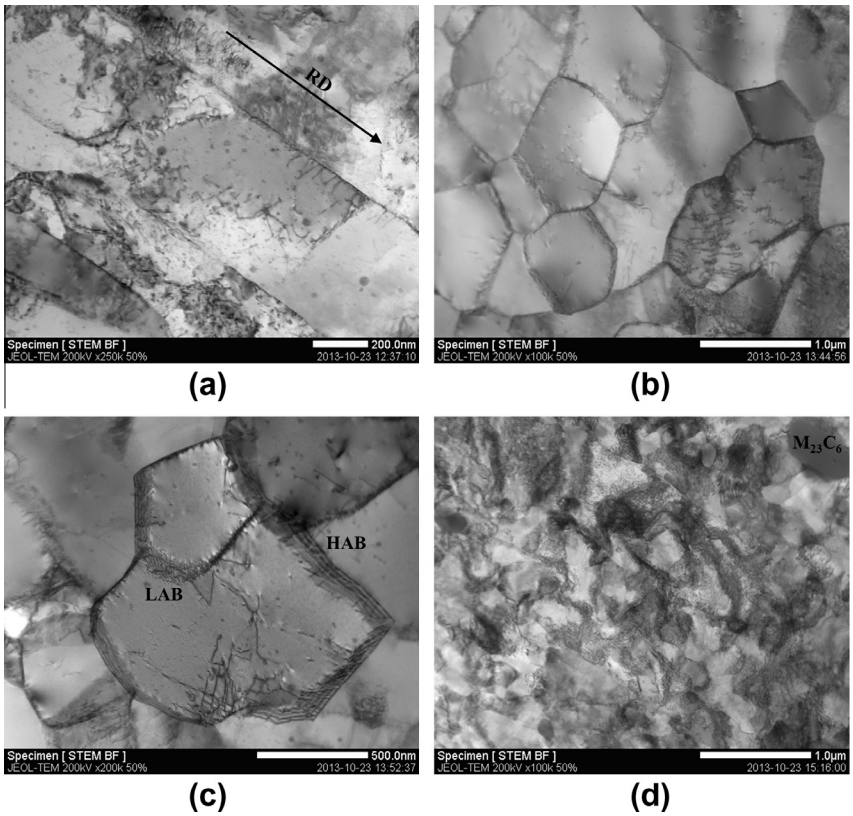

Fig. 2. Scanning transmission electron microscopy (STEM) bright field (BF) images of ODS-Eurofer steel annealed at 800 °C for 4320 h. The rolling direction (RD) shown in (a) is the same for all micrographs.

ing direction (RD). This feature is preserved during annealing at 800 °C (IPF maps in Fig. 4(b)–(d)) even after exposures at times as long as 4320 h. Recrystallized grains can be noticed in the annealed samples when a higher magnification is used (Fig 5). They can be distinguished from the deformed grains in the IPF maps because of their equiaxed morphology and for possessing orientations far from the neighboring deformed matrix. In the corresponding KAM maps (also Fig 5), they appear as tiny areas with low misorientation and their fraction increases with the annealing time (as shown in Fig 4). An increasing amount of large areas with low misorientations related to their neighbors are also noticed. According to the IPF maps, most of these large areas have similar orientations to the deformed matrix and high amounts of LABs. These areas are likely to be formed by static recovery, involving both the annihilation of individual dislocations and subgrain growth [46]. For the longest annealing time (4320 h), both types of areas with low KAM sum up to about 11% in total. Strongly recovered subgrains and recrystallized grains are included in this number. A higher volume fraction of recrystallized grains found mostly within γ-fiber grains (about 10%) have been reported

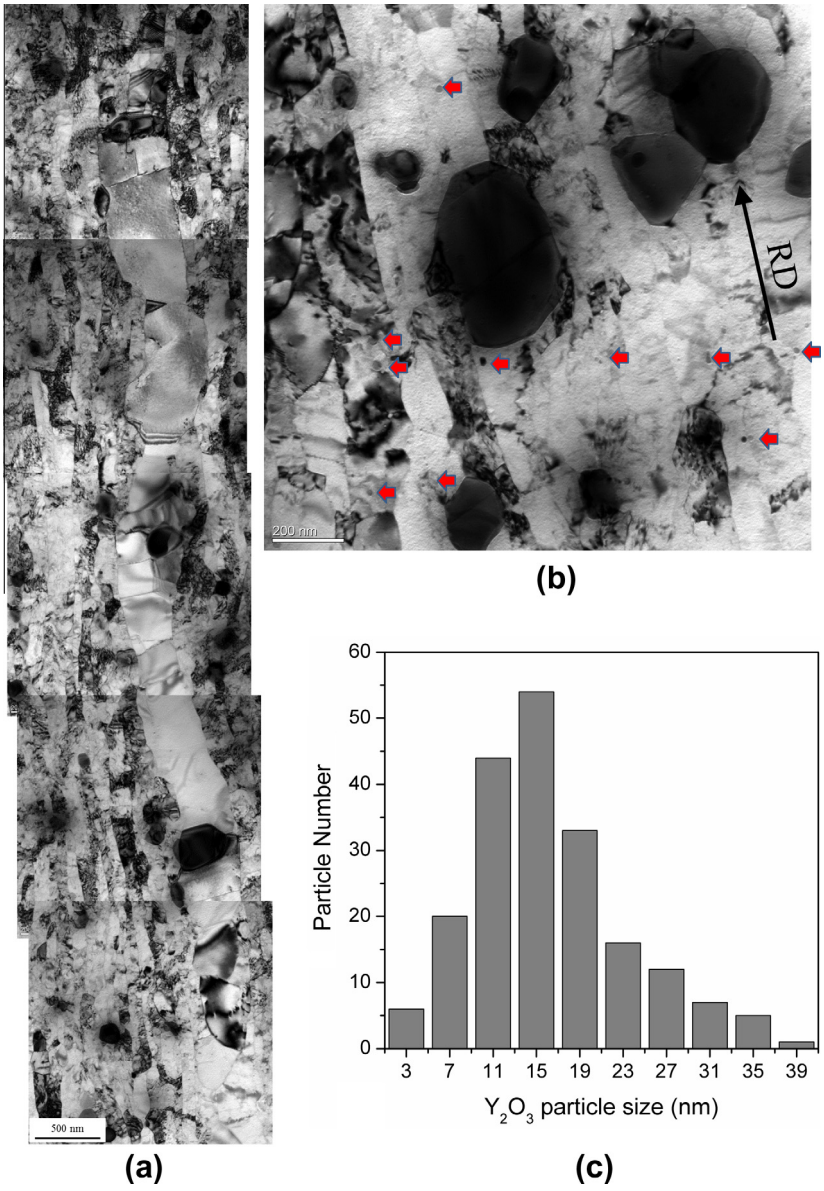

Fig. 3. (a) TEM montage of five consecutive bright field micrographs of ODS-Eurofer steel annealed at 800 °C for 4320 h; (b) Detail of coarse $M_{23}C_6$ particles and Y_2O_3 nanoparticles (red arrows); and (c) Y_2O_3 particle size distribution (bin width 4 nm). The RD is the same for both micrographs. (For interpretation of the references to color in this figure legend, the reader is referred to the web version of this article.)

elsewhere [35,47,48]. It is worth mentioning that larger areas have been used to evaluate the recrystallized volume fraction in Ref. [35].

Long-term annealing promotes minor changes in grain size distribution curves (Fig 6). The mean grain sizes for the material in the cold-rolled condition and after several annealing times are also indicated in Fig 6. From these values, it is clear that neither significant discontinuous recrystallization nor grain growth take place in ODS-Eurofer steel.

The most noticeable changes undergone by the material during annealing refer to the decrease of the volume fraction of LABs, as shown in Fig 7 where all misorientation distributions are plotted together to ease further comparison. The volume fraction of HABs for all annealing times did not change significantly. New HABs can be created during recovery when mobile dislocations are incorporated to the already-existing LABs with subsequent increase in misorientation. If the main softening mechanism were discontinuous recrystallization, a relatively sharp increase in the volume fraction of HABs would also be noticed [15,16]. These features are a compelling evidence of extended recovery as the predominant softening mechanism in this steel. Y_2O_3-particles are very effective to retard boundary migration during recrystallization [35]. Concurrently, static recovery reactions take place decreasing the driving force for boundary migration and subsequent growth of the nuclei. Local effects can explain why discontinuous recrystallization does not occur profusely in ODS-Eurofer steel, i.e. only nuclei with large curvatures surrounded by high amounts of stored energy, like those found at grain boundaries and deformation heterogeneities, are able to grow.

Fig. 8 shows the changes in texture during annealing of ODS-Eurofer steel at 800 °C. The deformation texture of the cold-rolled sample (Fig. 8a) consists of an incomplete α-fiber, i.e. grains with orientation ⟨1 1 0⟩ parallel to the RD, concentrated around the components {0 0 1}⟨1 $\bar{1}$ 0⟩ and {1 1 1} ⟨1 $\bar{1}$ 0 ⟩ and a complete γ fiber with {1 1 1}⟨1 1 0⟩ and {1 1 1}⟨1 1 2⟩ components having the stronger intensities, similarly to those found in other ferritic stainless steels

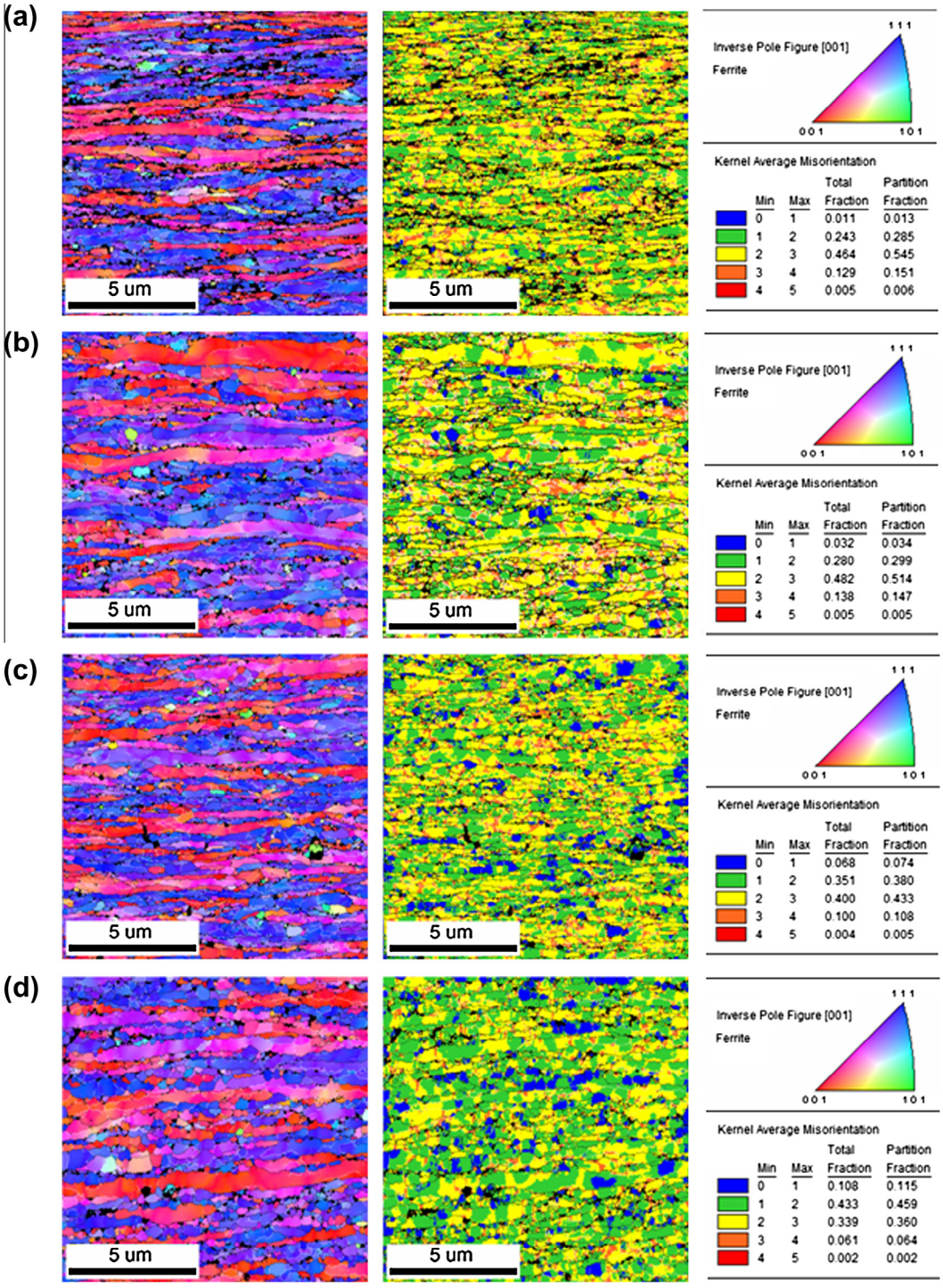

Fig. 4. EBSD mapping in longitudinal sections of ODS-Eurofer steel: (a) 80% cold-rolled; and after annealing in vacuum at 800 °C for (b) 1 h; (c) 1440 h; and (d) 4320 h. Left-handed images show the inverse pole figure maps and the right-handed images show the Kernel average misorientation maps. Black lines are HABs and grey lines mark LABs. The rolling direction (RD) is parallel to the scale bar.

[49–51]. The γ fiber refers to all grains with a common ⟨1 1 1⟩ axis parallel to the sheet normal. This texture is not only maintained but strengthened during annealing. Apart from the sample annealed for 4 months (Fig 8e), texture sharpening continuously increases with annealing time, as suggested by the increasing values of maximum intensity. This texture sharpening during annealing is reported in the literature for recovered and partially recrystallized materials and it may be attributed to static recovery [15,45,49,50].

3.2. Physical properties

In addition to the observation of the longitudinal sections of annealed specimens, the evaluation of other bulk physical properties is very useful to get a broader picture of the transformations that occur in the material [52–55]. Electrical and magnetic measurements, for instance, are especially useful to study the microstructural evolution since both are non-destructive and strongly affected by parameters as grain size, vacancy concentra-

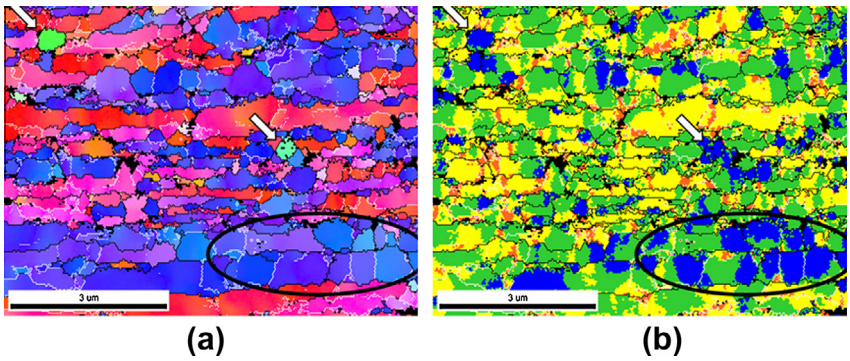

Fig. 5. EBSD maps in longitudinal sections of ODS-Eurofer after annealing at 800 °C for 4320 h: inverse pole figure maps (a) and Kernel average misorientation maps (b). Black lines are HABs and light grey lines are LABs. The rolling direction is parallel to the scale bar. The white arrows marks possible recrystallized grains and black ellipses mark recovered grains with low internal strain.

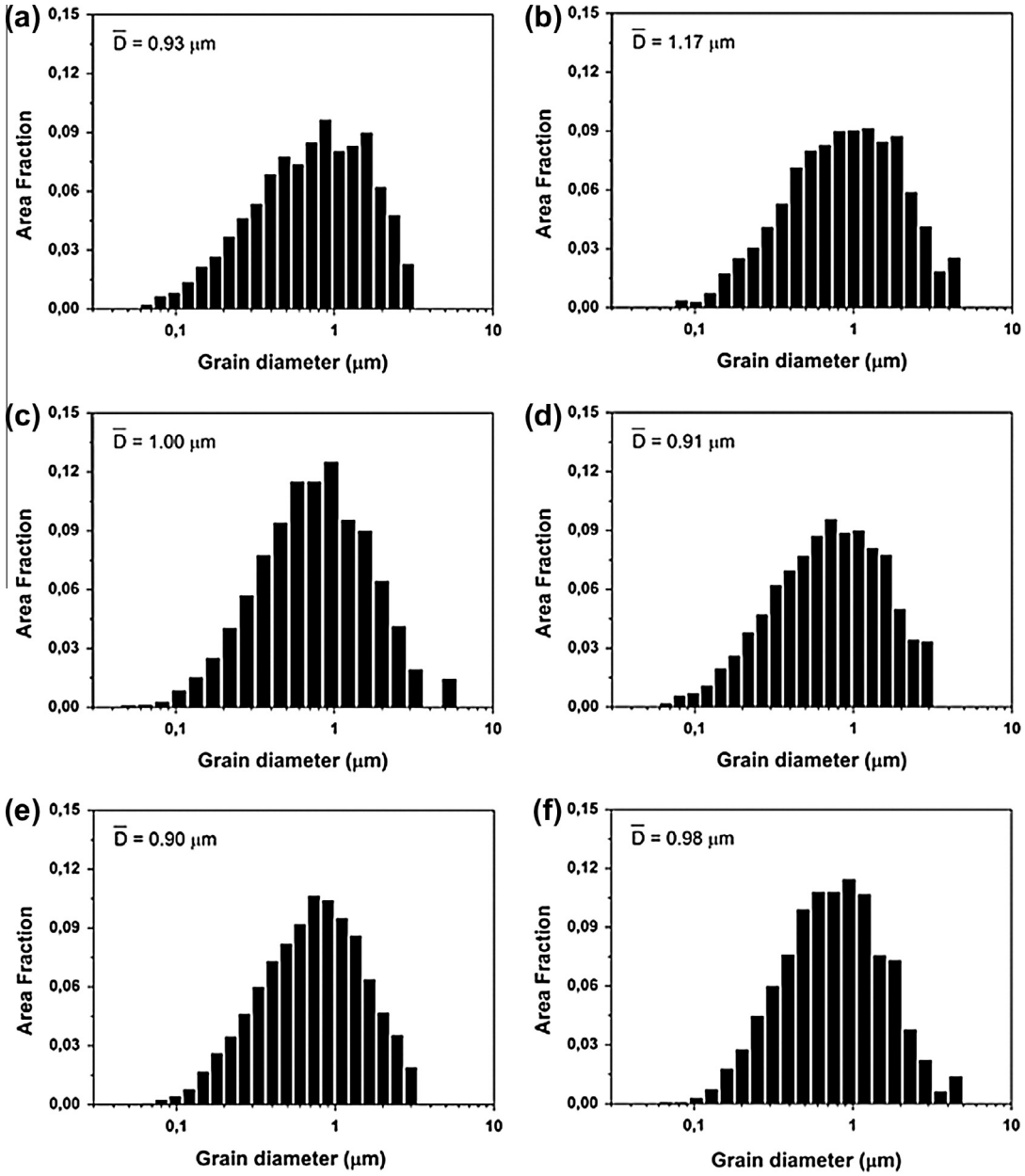

Fig. 6. Equivalent grain size distributions in ODS-Eurofer steel in: (a) 80% cold-rolled condition and after annealing in vacuum at 800 °C for (b) 1 h; (c) 720 h; (d) 1440 h, (e) 2880 h; and (f) 4320 h. $\overline{D}$ is the mean grain diameter for every metallurgical condition.

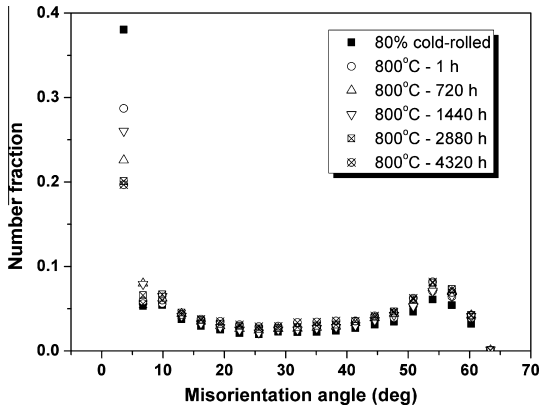

Fig. 7. Grain boundary misorientation distribution of ODS-Eurofer steels in the deformed state and after annealing at 800 °C for different lengths of time.

tion, dislocation density, and secondary phases [56–60]. The electrical resistivity of metal, for example, occurs due to the scattering of the conducting electrons specifically at solutes, interfaces, and dislocations, as they move within the material driven by the applied electrical potential. However, many sources of scattering may be present at the same time in a given material. The total resistivity would then be the sum of the individual resistivities caused by the different scattering sources, as stated in the *Matthiessen's rule* [61]. Considering the main scattering sources in metals (thermal vibration, lattice defects and solid solution impurities) the Matthiessen's rule can be simply written as:

$$\rho = \rho_T + \rho_d + \rho_i \tag{1}$$

where ρ is the total resistivity, and ρ_T, ρ_d, and ρ_i are the partial resistivities due to thermal phonons, crystalline defects, and impurities atoms, respectively. At high temperatures (e.g. above 100 K), thermal scattering is known to be the most expressed term while at very low temperatures (<10 K), ρ_T is much less significant and it can be suppressed in Eq. (1) [61]. Thus, the residual resistivity, ρ_R, depends mostly on terms ρ_d and ρ_i.

The coercive field (H_c), on the other hand, is a measure of the required energy to move the magnetic domain walls. A magnetic domain is a volume where the unbalanced electrons spins of a ferromagnetic phase have the same orientation. These magnetic interfaces can be pinned by crystalline defects, such as grain boundaries, second-phase particles, pores, dislocations, vacancies, and solid-solution atoms [62–64]. Thus, a lower grain size and a

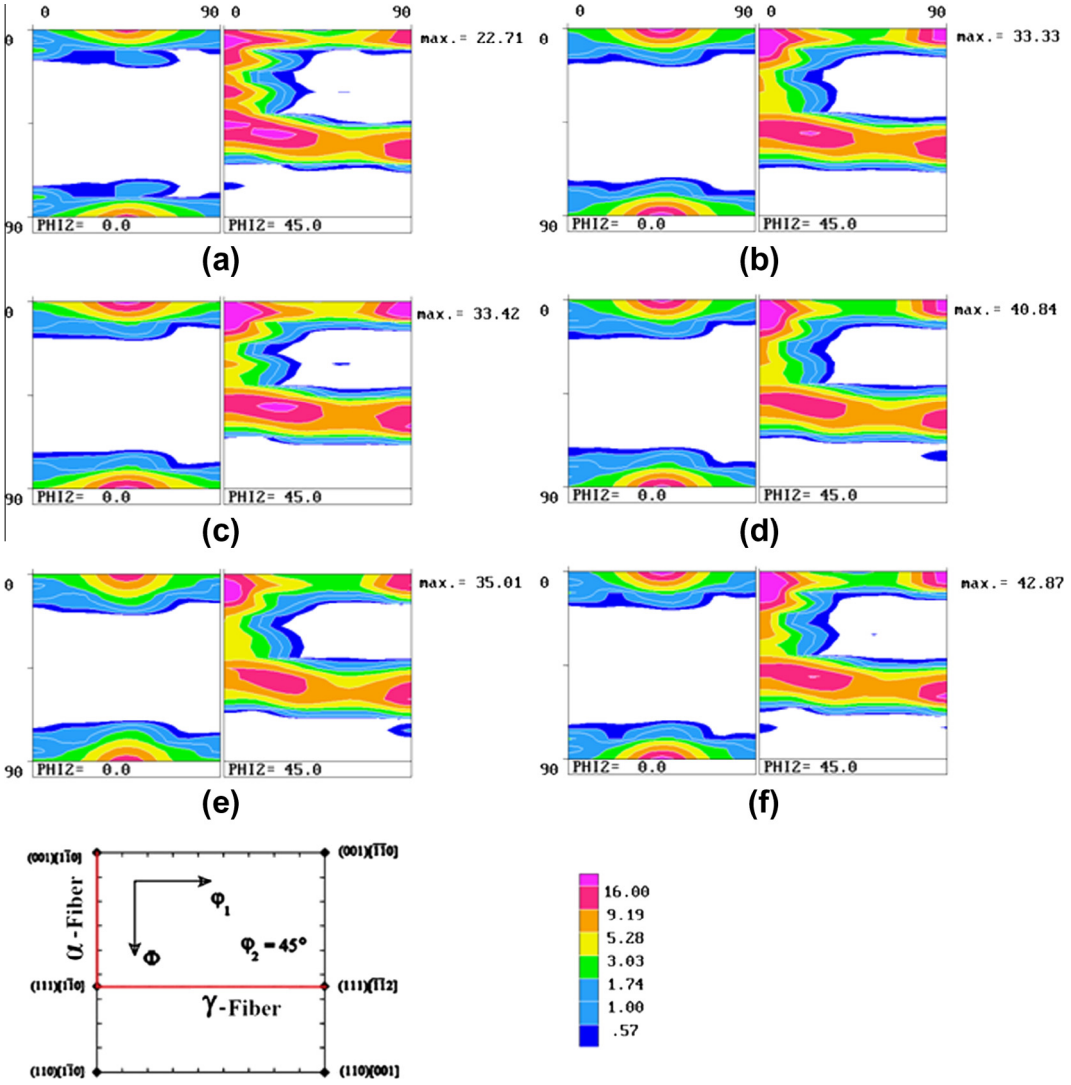

Fig. 8. Texture of ODS-Eurofer steel: a) 80% cold-rolled and following annealing at 800 °C for 1 h (b), 720 h (c), 1440 h (d), 2880 h (e) and 4320 h (f). Only sections of $\varphi_2 = 0°$ and $\varphi_2 = 45°$ are shown. The corresponding maximum intensities are also shown.

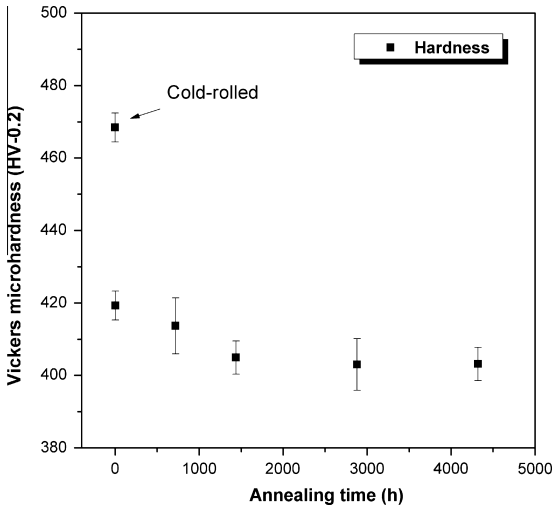

Fig. 9. Softening behavior of ODS-Eurofer steel followed by Vickers microhardness testing.

higher dislocation density are both expected to increase the values of the coercive field in a given material [59,60].

Fig 9 shows the softening kinetics of the ODS-Eurofer steel measured using Vickers hardness testing. Fig 10 shows the changes of ρ_R and H_c (both measured at 4 K) with annealing time. For the three properties evaluated in this investigation, most of the decrease is observed in the beginning of the annealing and longer annealing times did not promote any sharp transition. The maximum diminution of ρ_R is about 15% (from 0.208 to 0.170 μΩ m), very similar to the magnitude of the observed softening from 468 to 403 HV-0.2 (about 14%). In both cases, nearly all softening takes place during the first hour of annealing. The coercive field follows the same behavior. The cold-rolled material has H_c = 18.2 Oe while after 6 months at 800 °C H_c drops to 5.5 Oe. A low H_c is desirable for this material, since strong magnetic fields will be present in the first wall of the fusion reactors [65].

The similarity between the qualitative behavior of hardness, H_c and ρ_R can be readily understood when considering these three properties as motion indicators. The main aspect for the hardness is the mobility of dislocations, for the coercive field is the motion of domain walls and for resistivity is the mobility of conducting electrons. All these properties are strongly affected by the same microstructural features.

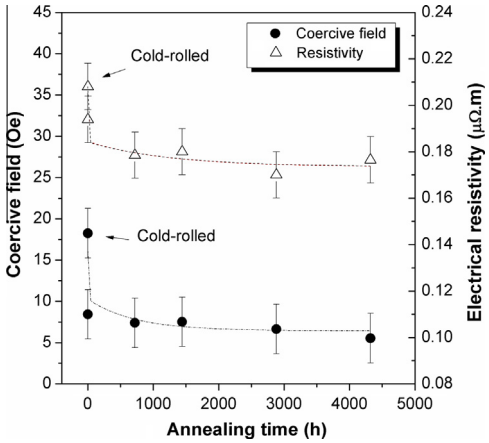

Fig. 10. Softening behavior of ODS-Eurofer steel followed by DC-magnetic coercive field and electrical resistivity measurements. Coercive field and electrical resistivity experimental errors are ±3 Oe and ± 0.01 μΩ m, respectively.

One-hour annealing at 800 °C promotes important changes in the microstructure of this steel caused by static recovery and discontinuous recrystallization. The observation that all of these properties level off after short annealing times (e.g. 1 h) is another evidence of the microstructural stability of this steel, i.e. the material does not undergo any significant microstructural changes for longer annealing times, in good agreement with the results of EBSD and texture measurements. For example, discontinuous recrystallization and grain growth could lead to a strong decrease in the values of these physical properties, as earlier reported by Oliveira et al. [18]. As reported in previous papers [17,35,66], Y_2O_3 particles exert effective pinning on high angles boundaries suppressing nucleation of discontinuous recrystallization [67].

Although the changes observed after long annealing times are very subtle and no larger than the standard deviation and experimental errors of the measurements, there seems to be a small tendency for a further decrease of the properties values with increasing annealing time, especially in hardness (Fig 9), in good agreement with the current theory on extended recovery [15]. Assuming that Y_2O_3 particles are stable at this temperature, the occurrence of extended recovery is more likely to be favored by further coarsening of carbide particles or local modifications in chemical composition.

In summary, it is worth stressing that these results show noticeable microstructural stability of ODS-Eurofer steel regarding discontinuous recrystallization at temperatures well-above those expected for steady-state conditions in fusion reactors but without neutron irradiation, since there are no facilities available to simulate the expected real operating conditions regarding neutron fluxes and energies yet.

4. Summary and conclusions

The microstructural stability of 80% cold-rolled ODS-Eurofer steel during isothermal annealing at 800 °C up to 4320 h (6 months) was investigated by means of several characterization techniques including EBSD, TEM, Vickers microhardness testing, XRD texture, low-temperature electrical resistivity, and DC-magnetic coercive field measurements. We draw the following conclusions:

(1) The major changes in the microstructure of this cold-rolled steel occur in the first hour of annealing at 800 °C. It can be noticed a significant decrease in the volume fraction of LABs when compared to the deformed material. Further decrease can be also noticed for longer annealing times primarily because of either dislocation annihilation or subgrain growth. This hypothesis is supported by the observed texture sharpening and the growth of larger low-misoriented areas in the Kernel average misorientation maps. Tiny equiaxed recrystallized grains can be also readily observed by TEM and EBSD just after the first hour of annealing at 800 °C. The volume fraction of recrystallized grains is about 10% after 4320 h.

(2) The grain size distributions are very similar for all metallurgical conditions investigated. The mean grain size for the cold-rolled material and for samples annealed for 1 h and 4320 h are 0.93 μm, 1.17 μm, and 0.98 μm, respectively.

(3) The softening kinetics was followed using Vickers hardness testing, magnetic, and electrical measurements. These three bulk properties show similar behaviors, i.e. a significant drop after annealing for 1 h followed by leveling off for longer annealing times. The major amount of softening in ODS-Eurofer steel takes places in the first hour of annealing at 800 °C (about 15%). Further softening occurs in this material due to extended recovery.

(4) Based on a limited number of particles observed in TEM (200 at all), the mean particle size of Y_2O_3 particles was found to be about 16 ±7 nm, close to the value reported for this steel in the starting (tempered) condition (12 nm). This result suggests that the oxide dispersion is fairly stable and very effective to retard primary recrystallization and further grain growth in ODS-Eurofer steel (Zener-Smith pinning) at this temperature.

Acknowledgments

Authors are grateful to the Brazilian funding agencies FAPESP (Grants 07/56.436-0, 09/54.001-2, and 11/07.109-2), CNPq (Grants 142.414/2011-5 and 473.903/2011-3), and CAPES (Grant PDSE 0254-13-4) for the financial support. Authors are also acknowledged to Mrs. Katja Angenendt (MPI-E, Düsseldorf) for her kind assistance in the EBSD measurements and to Dr. Michael Klimenkov for his assistance in TEM (CM-30 equipment).

References

[1] K. Ehrlich, Fusion Eng. Des. 56–57 (2001) 71–82.
[2] A. Kohyama, A. Hishinuma, D.S. Gelles, R.L. Klueh, W. Dietz, K. Ehrlich, J. Nucl. Mater. 233–237 (1996) 138–147.
[3] A. Hishinuma, A. Kohyama, R.L. Klueh, D.S. Gelles, W. Dietz, K. Ehrlich, J. Nucl. Mater. 258–263 (1998) 193–204.
[4] N. Baluc, R. Schäublin, P. Spätig, M. Victoria, Nucl. Fusion 44 (1) (2004) 56–61.
[5] R. Lindau, A. Möslang, M. Rieth, M. Klimiankou, E. Materna-Morris, A. Alamo, A.-A.F. Tavassoli, C. Cayron, A.-M. Lancha, P. Fernandez, N. Baluc, R. Schäublin, E. Diegele, G. Filacchioni, J.W. Rensman, B.v.d. Schaaf, E. Lucon, W. Dietz, Fusion Eng. Des. 75–79 (2005) 989–996.
[6] G. Yu, N. Nita, N. Baluc, Fusion Eng. Des. 75–79 (2005) 1037–1041.
[7] B. van der Schaaf, F. Tavassoli, C. Fazio, E. Rigal, E. Diegele, R. Lindau, G. LeMarois, Fusion Eng. Des. 69 (2003) 197–203.
[8] L.M. Giancarli, M. Abdou, D.J. Campbell, V.A. Chuyanov, M.Y. Ahn, M. Enoeda, C. Pan, Y. Poitevin, E. Rajendra Kumar, I. Ricapito, Y. Strebkov, S. Suzuki, P.C. Wong, M. Zmitko, Fusion Eng. Des. 87 (2012) 395–402.
[9] S.V. Rogozhkin, A. Aleev, A.G. Zaluzhnyi, A.A. Nikitin, N.A. Iskandarov, P. Vladimirov, R. Lindau, A. Möslang, J. Nucl. Mater. 409 (2) (2011) 94–99.
[10] M.J. Alinger, G.R. Odette, D.T. Hoelzer, J. Nucl. Mater. 329–333 (2004) 382–386.
[11] F.J. Humphreys, Met. Sci. 13 (1979) 136–145.
[12] A.O.F. Hayama, H.R.Z. Sandim, J.F.C. Lins, M.F. Hupalo, A.F. Padilha, Mater. Sci. Eng. A 371 (2004) 198–209.
[13] C. Zener, C.S. Smith, Trans AIME 175 (1948) 15.
[14] E. Nes, N. Ryum, O. Hunderi, Acta Metall. 33 (1) (1985) 11–22.
[15] F.J. Humphreys, M. Hatherly, Recrystallization and Related Annealing Phenomena, second ed., Elsevier, Oxford, 2004.
[16] R.D. Doherty, D.A. Hughes, F.J. Humphreys, J.J. Jonas, D. Juul Jensen, M.E. Kassner, W.E. King, T.R. McNelley, H.J. McQueen, A.D. Rollett, Mater. Sci. Eng. A 238 (2) (1997) 219–274.
[17] R.A. Renzetti, H.R.Z. Sandim, M.J.R. Sandim, A.D. Santos, A. Möslang, D. Raabe, Mater. Sci. and Eng. A 528 (3) (2011) 1442–1447.
[18] V.B. Oliveira, M.J.R. Sandim, D. Stamopoulos, R.A. Renzetti, A.D. Santos, H.R.Z. Sandim, J. Nucl. Mater. 435 (1–3) (2013) 189–195.
[19] A. Ramar, R. Schäublin, J. Nucl. Mater. 432 (1–3) (2013) 323–333.
[20] M. Rieth, M. Schirra, A. Falkenstein, P. Graf, S. Heger, H. Kempe, R. Lindau, H. Zimmermann, EUROFER 97, Tensile, Charpy, Creep and Structural Tests, Scientific Report, FZKA- 6911, Karlsruhe, 2003.
[21] P. Fernández, M. García-Mazarío, A.M. Lancha, J. Lapeña, J. Nucl. Mater. 329–333 (2004) 273–277.
[22] P. Fernández, A.M. Lancha, J. Lapeña, M. Serrano, M. Hernández-Mayoral, J. Nucl. Mater. 307–311 (2002) 495–499.
[23] R. Lindau, A. Möslang, M. Schirra, Fusion Eng. Des. 61–62 (2002) 659–664.
[24] R. Lindau, M. Schirra, Fusion Eng. Des. 58–59 (2001) 781–785.
[25] A. Czyrska-Filemonowicz, B. Dubiel, J. Mater. Proc. Technol. 64 (1997) 53–64.
[26] R. Lindau, A. Möslang, M. Schirra, P. Schlossmacher, M. Klimenkov, J. Nucl. Mater. 307–311 (2002) 769–772.
[27] V. de Castro, T. Leguey, M.A. Monge, A. Muñoz, R. Pereja, D.R. Amador, J.M. Torralba, M. Victoria, J. Nucl. Mater. 322 (2003) 228–234.
[28] M. Klimiankou, R. Lindau, A. Möslang, J. Nucl. Mater. 367–370 (2007) 173–178.
[29] R. Song, D. Ponge, R. Kaspar, D. Raabe, Z. Metallk 95 (2004) 513–517.
[30] R. Song, D. Ponge, D. Raabe, R. Kaspar, Acta Mater. 53 (2004) 845–858.
[31] J.S. Kallend, U.F. Kocks, A.D. Rollett, H.R. Wenk, Texture Microstruct. 14–18 (1991) 1203–1208.
[32] Y.B. Cai, S.K. Chang, ISIJ Int. 47 (2007) 1680–1686.
[33] R. Schaeublin, T. Leguey, P. Spätig, N. Baluc, M. Victoria, J. Nucl. Mater. 307–311 (2002) 778–782.
[34] M. Klimiankou, R. Lindau, A. Möslang, J. Nucl. Mater. 329–333 (2004) 347–351.
[35] H.R.Z. Sandim, R.A. Renzetti, A.F. Padilha, D. Raabe, M. Klimenkov, R. Lindau, A. Möslang, Mater. Sci. Eng. A 527 (2010) 3602–3608.
[36] K. Zilnyk, H.R.Z. Sandim, G.C. Coelho, A. Möslang, Phase stability of Ta-containing reduced-activation ferritic-martensitic steel. Paper presented at CALPHAD XLII, San Sebsatian, Spain, 26–31 May 2013, pp. 108.
[37] L. Zhang, S. Ukai, T. Hoshino, S. Hayashi, X. Qu, Acta Mater. 57 (2009) 3671–3682.
[38] C. Capdevila, Metall. Mater. Trans. A 36 (2005) 1547–1555.
[39] M. Klimiankou, R. Lindau, A. Moslang, J. Cryst Growth 249 (1–2) (2003) 381–387.
[40] Z. Oksiuta, P. Kozikowski, M. Lewandowska, M. Ohnuma, K. Suresh, K.J. Kurzydlowski, J. Mater. Sci. 48 (13) (2013) 4620–4625.
[41] J. Ribis, Y. De Carlan, Acta Mater. 60 (2012) 238–252.
[42] C.A. Williams, G.D.W. Smith, E.A. Marquis, Scripta Mater. 67 (2012) 108–111.
[43] Ch.Ch. Eiselt, M. Klimenkov, R. Lindau, A. Möslang, H.R.Z. Sandim, A.F. Padilha, D. Raabe, J. Nucl. Mater. 385 (2) (2009) 231–235.
[44] M. Calcagnotto, D. Ponge, D. Raabe, Mater. Sci. Eng. A 527 (2010) 2738–2746.
[45] I. Thomas, S. Zaefferer, F. Friedel, D. Raabe, Adv. Eng. Mater. 5 (2003) 566–570.
[46] D. Raabe, Steel Res. 66 (1995) 222–229.
[47] D. Raabe, K. Lücke, Scripta Metall. 26 (1992) 19–24.
[48] D. Raabe, K. Lücke, Steel Res. 63 (1992) 457–464.
[49] M. Hölscher, D. Raabe, K. Lücke, Steel Res. 62 (1991) 567–575.
[50] D. Raabe, K. Lücke, Scripta Metall. 27 (1992) 1533–1538.
[51] D. Raabe, K. Lücke, Mater. Sci. Technol. 9 (1993) 302–312.
[52] A. Desalvo, F. Zignani, J. Nucl. Mater. 20 (1966) 108–118.
[53] W. Hibbard, Acta Metall. 7 (1959) 565–574.
[54] H. Dawson, Acta Metall. 12 (1964) 113–116.
[55] W. Aarts, R. Jarvis, Acta Metall. 2 (1954) 87–91.
[56] J.S. Park, Y.K. Lee, Scripta Mater. 56 (2007) 225–228.
[57] O.S. Es-Said, J.G. Morris, R.J. De Angelis, Mater. Charact. 30 (1993) 113–125.
[58] S.P. Chaudhuri, R.K. Mahanti, C.S. Sivaramakrishnan, M.P. Singh, Mater. Des. 23 (2002) 489–496.
[59] A. Martínez-de-Guerenu, F. Arizti, M. Dias-Fuentes, I. Gutiérrez, Acta Mater. 52 (2004) 3657–3664.
[60] M. Oyarzábal, K. Gurruchaga, A. Martínez-de-Guerenu, I. Gutiérrez, ISIJ Int. 47 (2007) 1458–1464.
[61] C. Kittel, Introduction to Solid State Physics, eighth ed., John Wiley & Sons, Hoboken, 2004.
[62] B.D. Cullity, Introduction to Magnetic Materials, Addison-Wesley, Boston, 1972.
[63] M.J. Sablik, J. Appl. Phys. 89 (2001) 7254–7256.
[64] E. Arzt, Acta Mater. 46 (1998) 5611–5626.
[65] S. Jitsukawa, M. Tamura, B. van der Schaaf, R.L. Klueh, A. Alamo, C. Petersen, M. Schirra, P. Spätig, G.R. Odette, A.A. Tavassoli, K. Shiba, A. Kohyama, A. Kimura, J. Nucl. Mater. 307–311 (2002) 179–186.
[66] H.R.Z. Sandim, A.O. Hayama, D. Raabe, Mat. Sci. Eng. A 430 (2006) 172–178.
[67] D. Raabe, L. Hantcherli, Comput. Mater. Sci. 34 (2005) 299–313.